Usher type 1G protein sans is a critical component of the tip-link complex, a structure controlling actin polymerization in stereocilia.

Elisa Caberlotto, Michel Vittot, Isabelle Foucher, Amel Bahloul, Richard J Goodyear, Elise Pepermans, Nicolas Michalski, Isabelle Perfettini, O. Alegria-Prevot, Sébastien Chardenoux, et al.

Usher type 1G protein sans is a critical component of the tip-link complex, a structure controlling actin polymerization in stereocilia

Elisa Caberlotto[a,b,c], Vincent Michel[a,b,c], Isabelle Foucher[a,b,c,1], Amel Bahloul[a,b,c], Richard J. Goodyear[d], Elise Pepermans[a,b,c], Nicolas Michalski[a,b,c], Isabelle Perfettini[a,b,c], Olinda Alegria-Prévot[a,b,c], Sébastien Chardenoux[a,b,c], Marcio Do Cruzeiro[e], Jean-Pierre Hardelin[a,b,c], Guy P. Richardson[d], Paul Avan[f], Dominique Weil[a,b,c], and Christine Petit[a,b,c,g,2]

[a]Unité de Génétique et Physiologie de l'Audition, Institut Pasteur, 75724 Paris cedex 15, France; [b]Institut National de la Santé et de la Recherche Médicale Unité Mixte de Recherche en Santé, 587, 75015 Paris, France; [c]Université Pierre et Marie Curie, 75015 Paris, France; [d]School of Life Sciences, University of Sussex, Falmer, Brighton BN1 9QG, United Kingdom; [e]Plate-Forme de Recombinaison Homologue, Université Paris Descartes, Institut National de la Santé et de la Recherche Médicale Unité Mixte de Recherche en Santé, 1016, Centre National de la Recherche Scientifique Unité Mixte de Recherche, 8104, Institut Cochin, 75014 Paris, France; [f]Laboratoire de Biophysique Sensorielle, Faculté de Médecine, Université d'Auvergne, F-63001 Clermont-Ferrand, France; and [g]Collège de France, 75005 Paris, France

Edited* by Elaine Fuchs, The Rockefeller University, New York, NY, and approved February 24, 2011 (received for review November 18, 2010)

The mechanotransducer channels of auditory hair cells are gated by tip-links, oblique filaments that interconnect the stereocilia of the hair bundle. Tip-links stretch from the tips of stereocilia in the short and middle rows to the sides of neighboring, taller stereocilia. They are made of cadherin-23 and protocadherin-15, products of the Usher syndrome type 1 genes USH1D and USH1F, respectively. In this study we address the role of sans, a putative scaffold protein and product of the USH1G gene. In *Ush1g*$^{-/-}$ mice, the cohesion of stereocilia is disrupted, and both the amplitude and the sensitivity of the transduction currents are reduced. In *Ush1g*$^{fl/fl}$*Myo15-cre*$^{+/-}$ mice, the loss of sans occurs postnatally and the stereocilia remain cohesive. In these mice, there is a decrease in the amplitude of the total transducer current with no loss in sensitivity, and the tips of the stereocilia in the short and middle rows lose their prolate shape, features that can be attributed to the loss of tip-links. Furthermore, stereocilia from these rows undergo a dramatic reduction in length, suggesting that the mechanotransduction machinery has a positive effect on F-actin polymerization. Sans interacts with the cytoplasmic domains of cadherin-23 and protocadherin-15 in vitro and is absent from the hair bundle in mice defective for either of the two cadherins. Because sans localizes mainly to the tips of short- and middle-row stereocilia in vivo, we conclude that it belongs to a molecular complex at the lower end of the tip-link and plays a critical role in the maintenance of this link.

auditory mechanoelectrical transduction | Usher syndrome type 1 | deafness | conditional knockout mice | organ of Corti

In the sensory hair cells of the auditory system, the hair bundle converts acoustic energy into an electrical receptor potential. The hair bundle is a morphologically and functionally polarized ensemble of stiff microvilli (stereocilia) that are arranged into three height-ranked rows forming a V- or U-shaped staircase pattern. Developing hair bundles also contain a genuine cilium, the kinocilium. Identification of the genes defective in Usher syndrome type 1 (USH1)—a disease characterized by congenital profound deafness, vestibular dysfunction, and delayed-onset retinopathy leading to blindness—has revealed the cohesive role of the transient fibrous lateral links that interconnect the stereocilia and connect the kinocilium to the stereocilia early in development (1). These links are made of two Ca^{2+}-dependent adhesion molecules, the transmembrane proteins cadherin-23 and protocadherin-15 (2, 3), which are defective in the USH1D and USH1F (4) genetic forms, respectively. The tip-link (5, 6), a single oblique link running from the tip of one stereocilium to the side of its taller neighbor, also consists of cadherin-23 and protocadherin-15, which make up its upper and lower parts, respectively (7–9). According to the prevailing model for mechanoelectrical transduction, tip-link tension controls the open probability of one or two mechanoelectrical transduction (MET) channels in each stereocilium (10). These channels are located at the lower insertion point of the tip-link (11), i.e., at the very tips of stereocilia in the short and medium rows.

The other USH1 genes encode myosin VIIa (USH1B), the PDZ-domain–containing submembrane protein harmonin (USH1C), and another putative scaffold protein called sans (USH1G) (1). The direct in vitro interactions between the five USH1 proteins (2, 12–16) and the colocalization of cadherin-23, protocadherin-15, myosin VIIa, and harmonin in the growing hair bundle, along with the common early morphological defect in cochlear hair bundles of mouse mutants defective for any USH1 gene (17), suggest that USH1 proteins cooperate in hair bundle development. It has been proposed that harmonin-b anchors transient fibrous lateral links to the stereocilia actin filaments and that myosin VIIa creates tension on these links (2, 16), but the role played by sans is still unknown. Sans directly interacts in vitro with both the myosin VIIa tail (13) and harmonin (13, 18), but has so far not been detected within the hair bundle (13), thus questioning its participation in the USH1 molecular network that underlies cohesion of the growing hair bundle. To elucidate the role of sans, we studied the morpho-functional characteristics of the hair bundle in early ubiquitous and delayed conditional *Ush1g* knockout mice that lack sans from the early stages of hair cell development and in the later stages of hair bundle differentiation, respectively.

Results and Discussion

Mechanoelectrical Transduction Currents Are Defective in Cochlear and Vestibular Hair Cells of *Ush1g*$^{-/-}$ Mice. The 460-amino-acid putative scaffolding protein sans contains a series of three ankyrin repeats and a sterile α-motif (SAM) domain, with an intervening a 95-aa central region (CENT) and a C-terminal

Author contributions: E.C. and C.P. designed research; E.C., V.M., I.F., A.B., R.J.G., E.P., N.M., I.P., O.A.-P., S.C., M.D.C., P.A., and D.W. performed research; E.C., V.M., I.F., A.B., G.P.R., P.A., D.W., and C.P. analyzed data; and E.C., J.-P.H., and C.P. wrote the paper.

The authors declare no conflict of interest.

*This Direct Submission article had a prearranged editor.

Freely available online through the PNAS open access option.

[1]Present address: Institut de Neurobiologie Alfred Fessard, CNRS, F-91198 Gif-sur-Yvette, France.

[2]To whom correspondence should be addressed. E-mail: christine.petit@pasteur.fr.

This article contains supporting information online at www.pnas.org/lookup/suppl/doi:10.1073/pnas.1017114108/-/DCSupplemental.

PDZ domain-binding consensus motif. The previously described *Ush1g* mutant mice (*js/js* mice), which display profound deafness and a balance defect, have nucleotide insertions (19) that may result in a protein truncated just upstream or at the beginning of the SAM domain. These mutants may therefore not be appropriate to explore the consequences of the absence of sans in the inner ear. To produce bona fide sans-null ($Ush1g^{-/-}$) mice, we first engineered $Ush1g^{fl/fl}$ mice by targeting exon 2 (Fig. S1*A*). These mice were then crossed with *PGK-cre* mice (20).

Sound processing in the cochlea involves two types of sensory cells: specifically, the inner hair cells (IHCs), which are the genuine sensory cells that release neurotransmitters and induce action potentials in afferent neurons, and the outer hair cells (OHCs), which locally amplify the sound-induced motion of the sensory epithelium. Exploration of the auditory functions of $Ush1g^{-/-}$ mice in vivo showed a lack of identifiable auditory brainstem response (ABR) waves for all sound frequencies even at the highest intensity (105 dB SPL) tested. In addition, distortion-product otoacoustic emissions (DPOAEs) and cochlear microphonics (CM) were not detected in these mice (Fig. S2*C*), thus establishing the loss of OHC activity. IHC and OHC hair bundles of postnatal day 5 (P5) $Ush1g^{-/-}$ mice analyzed using scanning EM showed a disorganization of the stereocilia reminiscent of that observed in the *js/js* mutant mice (17). Notably, OHC hair bundles were often fragmented in two or more clumps of stereocilia, and their kinocilia were mispositioned (Fig. S3).

We analyzed the MET currents as a function of hair bundle displacement in cochlear and vestibular hair cells from $Ush1g^{fl/fl}$ and $Ush1g^{-/-}$ mice at P5 and P1, respectively, i.e., several days after the onset of MET in the two sensory organs (21–23). The maximal amplitudes of MET currents were markedly reduced in IHCs and OHCs from P5 $Ush1g^{-/-}$ mice (51 ± 9 pA in IHCs, 91 ± 24 pA in OHCs) compared with $Ush1g^{fl/fl}$ control mice (471 ± 40 pA in IHCs, 696 ± 50 pA in OHCs; unpaired *t* test, $P < 10^{-4}$ for both comparisons), and the average sensitivity of the MET currents to hair bundle displacement was decreased by ~50% in both IHCs and OHCs as well (unpaired *t* test, $P < 10^{-4}$) (Fig. S3). Both MET current abnormalities could result from the morphologically abnormal hair bundles in these mice (Fig. S3). In contrast, residual MET current could not be detected in IHCs and OHCs from P5 cadherin-23-null ($Cdh23^{-/-}$) mice (24) that lack tip-links (Fig. S4*A*). We then analyzed the MET currents in utricular hair cells (UHCs) of the vestibule from P1 $Ush1g^{-/-}$ mice. Notably, not all of the UHC hair bundles were fragmented, and MET current recordings were performed on selected cells that displayed morphologically intact hair bundles. The maximal amplitudes of the MET current in $Ush1g^{-/-}$ UHCs (88 ± 12 pA) were 30% those of $Ush1g^{fl/fl}$ UHCs (295 ± 30 pA) (unpaired *t* test, $P < 10^{-4}$) (Fig. 1*A*). The normalized $P_o(X)$ curves, however, superimposed, indicating the lack of change in the sensitivity of the MET machinery in the UHCs from $Ush1g^{-/-}$ mice. Accordingly, the hair bundle displacement eliciting half of the maximal MET current ($X_{0.5}$) was the same in the mutant and control UHCs (unpaired *t* test, $P = 0.08$ and $P = 0.06$, respectively). The results obtained in morphologically intact $Ush1g^{-/-}$ UHCs thus suggest that sans plays a role in the MET machinery. The fact that we found residual MET currents in the vestibular and cochlear $Ush1g^{-/-}$ hair cells at P1 and P5, respectively, however, indicates that sans is dispensable for the initial assembly of the MET machinery.

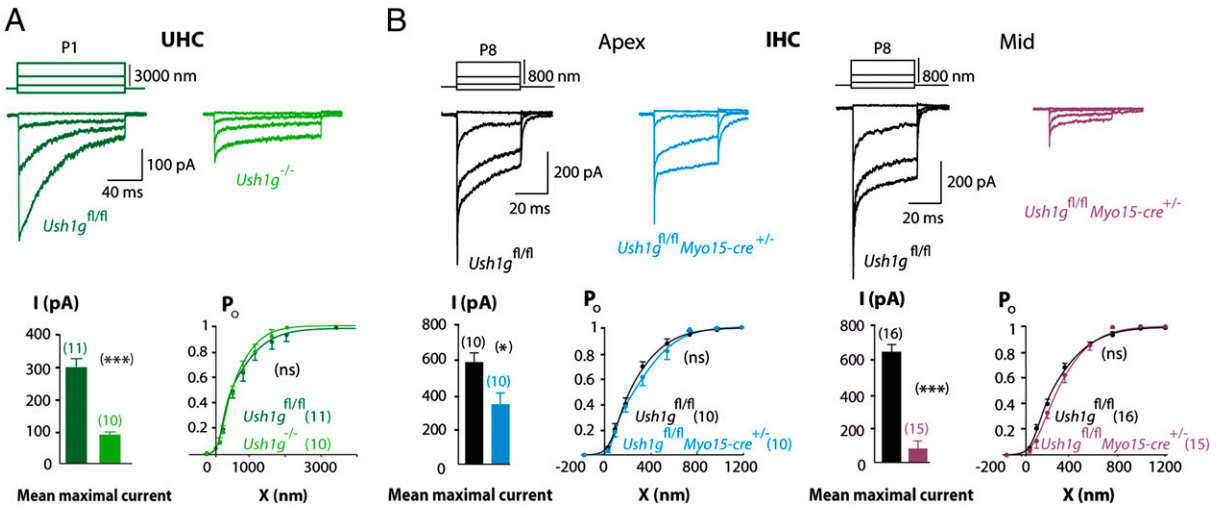

Fig. 1. (*A*) Mechanoelectrical transduction current recordings in UHCs from $Ush1g^{-/-}$ P1 mice. In the graduated shading of green, examples of transduction current recordings in UHCs from $Ush1g^{fl/fl}$ and $Ush1g^{-/-}$ P1 mice are shown. Mean maximum amplitudes are 295 ± 30 pA and 88 ± 23 pA in $Ush1g^{fl/fl}$ and $Ush1g^{-/-}$ UHCs, respectively (unpaired *t* test, $P < 10^{-4}$). $P_o(X)$ curves plotted for $Ush1g^{fl/fl}$ and $Ush1g^{-/-}$ UHCs can be superimposed, with average sensitivity values of 0.88 ± 0.11 μm^{-1} and 1.18 ± 0.21 μm^{-1} for $Ush1g^{fl/fl}$ and $Ush1g^{-/-}$ UHCs, respectively (unpaired *t* test, $P = 0.08$). No change in $X_{0.5}$ can be detected in the mutant UHCs ($X_{0.5}$ = 686 ± 138 nm and 620 ± 75 nm for $Ush1g^{fl/fl}$ and $Ush1g^{-/-}$ UHCs, respectively; unpaired *t* test, $P = 0.06$). (*B*) Mechanoelectrical transduction currents were recorded in IHCs from $Ush1g^{fl/fl}Myo15\text{-}cre^{+/-}$ P8 mice. We analyzed mechanoelectrical transduction currents in cochlear inner hair cells from the apical region (~35% of the total length of the cochlea from the apex) and the middle region (~55% of the total length) of the cochlea in $Ush1g^{fl/fl}$ and $Ush1g^{fl/fl}Myo15\text{-}cre^{+/-}$ P8 mice. (*Left*) Examples of transduction currents in apical IHCs from $Ush1g^{fl/fl}$ (black) and $Ush1g^{fl/fl}Myo15\text{-}cre^{+/-}$ (blue) mice. Mean maximum current amplitude is 584 ± 52 pA and 346 ± 71 pA for $Ush1g^{fl/fl}$ and $Ush1g^{fl/fl}Myo15\text{-}cre^{+/-}$ IHCs, respectively (unpaired *t* test, $P = 0.015$). The $P_o(X)$ curves, however, can be superimposed with average sensitivity values of 1.85 ± 0.16 μm^{-1} and 1.72 ± 0.15 μm^{-1} for $Ush1g^{fl/fl}$ and $Ush1g^{fl/fl}Myo15\text{-}cre^{+/-}$ IHCs, respectively (unpaired *t* test, $P = 0.58$). In addition, no change in $X_{0.5}$ can be detected in the mutant IHCs ($X_{0.5}$ = 218 ± 13 nm and 421 ± 109 nm for $Ush1g^{fl/fl}$ and $Ush1g^{fl/fl}Myo15\text{-}cre^{+/-}$ IHCs, respectively; unpaired *t* test, $P = 0.08$). (*Right*) Examples of transduction currents in $Ush1g^{fl/fl}$ and $Ush1g^{fl/fl}Myo15\text{-}cre^{+/-}$ IHCs from the middle of the cochlea at P8. Mean maximum current amplitude is 652 ± 44 pA and 84 ± 44 pA for $Ush1g^{fl/fl}$ and $Ush1g^{fl/fl}Myo15\text{-}cre^{+/-}$ IHCs, respectively (unpaired *t* test, $P < 10^{-4}$). The $P_o(X)$ curves, however, can be superimposed with average sensitivity values of 1.95 ± 0.12 μm^{-1} and 2.00 ± 0.61 μm^{-1} for $Ush1g^{fl/fl}$ and $Ush1g^{fl/fl}Myo15\text{-}cre^{+/-}$ IHCs, respectively (unpaired *t* test, $P = 0.94$). In addition, no change in $X_{0.5}$ can be detected in the mutant IHCs ($X_{0.5}$ =220 ± 19 nm and 489 ± 122 nm in $Ush1g^{fl/fl}$ and $Ush1g^{fl/fl}Myo15\text{-}cre^{+/-}$ mice, respectively; unpaired *t* test, $P = 0.07$).

$Ush1g^{fl/fl}Myo15\text{-}cre^{+/-}$ Mice Are Profoundly Deaf and Develop a Balance Defect. To circumvent the early morphogenetic defect present in the hair bundles of $Ush1g^{-/-}$ mice, we engineered $Ush1g^{fl/fl}Myo15\text{-}cre^{+/-}$ mutant mice, in which *Ush1g* was deleted postnatally. These mice were obtained by crossing $Ush1g^{fl/fl}$ mice with $Myo15\text{-}cre^{+/-}$ mice in which cre recombinase gene expression was driven by the *Myo15a* promoter (Fig. S1*B*). The presence of the *Myo15-cre* allele leads to the sequential inactivation of a *lacZ* reporter gene from the basal to the apical region of the cochlea, starting at P0 at the base (Fig. S1*C*). ABRs, DPOAEs, and CM were analyzed in $Ush1g^{fl/fl}Myo15\text{-}cre^{+/-}$ mice at P13, P15, and P21 (Fig. S2). At P13, these mice lacked identifiable ABR waves for all sound frequencies, even at the highest intensity tested (105 dB SPL). This indicates that IHCs are impaired because even a complete loss of OHC function cannot account for more than a 60-dB threshold elevation (25). In the P13 mutant mice, the round-window CM in response to sound stimulation could not be detected either, thus indicating that the high-frequency OHCs from the basal end of the cochlea were severely impaired. Moreover, the DPOAE amplitudes at 15 kHz did not significantly differ from background noise at all sound intensities tested, thus indicating that the OHC functional defect extends to cells tuned to this lower frequency. DPOAE amplitudes at 10 kHz were, however, still close to those obtained in $Ush1g^{fl/fl}$ P13 mice in response to 70 dB SPL stimuli, indicating partly preserved OHC function at this lower frequency (Fig. S2*A*). From P15 onward, neither CMs nor DPOAEs could be recorded in $Ush1g^{fl/fl}Myo15\text{-}cre^{+/-}$ mice at all sound intensities and frequencies tested, indicating that the activity of all OHCs was now severely impaired (Fig. S2*B*). Notably, these mice also displayed a progressive vestibular dysfunction starting at P21, as assessed by their circling behavior and abnormal vestibular tests (26).

Amplitude of MET Currents Is Reduced in IHCs from $Ush1g^{fl/fl}Myo15\text{-}cre^{+/-}$ Mice. We studied the MET currents in hair cells from $Ush1g^{fl/fl}Myo15\text{-}cre^{+/-}$ mice. Recordings were performed in $Ush1g^{fl/fl}Myo15\text{-}cre^{+/-}$ and $Ush1g^{fl/fl}$ mice at positions located in the apical end (at ~35% the total length of the cochlea from its apex) and in the middle (~55% the total length) of the cochlea. At P7, at both cochlear sites, MET currents in IHCs and OHCs of $Ush1g^{fl/fl}Myo15\text{-}cre^{+/-}$ mice were indistinguishable from those of $Ush1g^{fl/fl}$ mice (Fig. S5). In contrast, P8 $Ush1g^{fl/fl}Myo15\text{-}cre^{+/-}$ IHCs displayed a decrease in the maximal amplitude of their MET current. At the apex and middle of the cochlea, the maximal amplitudes in $Ush1g^{fl/fl}Myo15\text{-}cre^{+/-}$ mice (346 ± 71 pA and 84 ± 44 pA, respectively) were on average 60% and 13% those of IHCs from $Ush1g^{fl/fl}$ mice (584 ± 52 pA and 652 ± 44 pA; unpaired *t* test, $P = 0.015$ and $P < 10^{-4}$), respectively (Fig. 1*B*). The $P_o(X)$ curves of $Ush1g^{fl/fl}Myo15\text{-}cre^{+/-}$ and $Ush1g^{fl/fl}$ IHCs at both cochlear sites could, however, be superimposed, thus indicating that the MET sensitivity to hair bundle displacement is preserved. We then investigated the characteristics of MET current adaptation, the process that resets the sensitivity of the MET channel close to its normal resting value during sustained stimuli. No changes were observed in the extent of adaptation or the kinetics when analyzed in IHCs from apical cochlear regions (Fig. S6). Therefore, the lack of sans in IHCs affects only the amplitude of the MET current without affecting the sensitivity of the hair bundle to displacement or adaptation. This suggests that the MET machinery functions normally in some of the stereocilia, but ~40% and 87% of the MET complexes are entirely nonfunctional at the apex and at the mid region of the cochlea, respectively. The role of sans in the MET process thus markedly differs from that of harmonin-b, which is involved in the extent of adaptation but does not play a significant role in the amplitude of the MET current (22). No difference in the OHC MET currents could be detected between $Ush1g^{fl/fl}Myo15\text{-}cre^{+/-}$ and $Ush1g^{fl/fl}$ P8 mice (Fig. S7).

Disappearance of the Tip-Links and Reduction of Stereocilia Height from the Small and Middle Rows in $Ush1g^{fl/fl}Myo15\text{-}cre^{+/-}$ Mice. We analyzed the structure of the hair bundles in IHCs and OHCs from the apical and middle regions of the cochlea in $Ush1g^{fl/fl}Myo15\text{-}cre^{+/-}$ mice at P8, P9, and P22 by scanning EM. At P8, hair bundles of IHCs from the apical region were cohesive with a normal U shape, and the tip-links could be detected and had prolate-shaped tips, a form thought to result from the tension exerted on the stereocilia tips by tip-links (27). In the mid region, however, only a few prolate-shaped stereocilia tips (<10%) and tip-links were observed within the medium row of stereocilia (Figs. 2 and 3). In contrast, the $Ush1g^{fl/fl}Myo15\text{-}cre^{+/-}$ OHC hair bundles could not be distinguished from the $Ush1g^{fl/fl}$ ones on this day (Fig. 2). At P9, additional hair bundle anomalies appeared in the mutant IHCs from the middle to the apex of the cochlea; specifically, some stereocilia within the small and medium rows had reduced heights (Figs. 2 and 3). These features were also present in mutant OHCs from the cochlear base. At P22, the reduction of the stereocilia length was much more pronounced, and some of the stereocilia from the small row had even disappeared in both the IHCs and the OHCs throughout the cochlea. Notably, the size of the stereocilia that compose the tallest row was unchanged in the mutants.

These observations suggested that the tip-link and/or the tip-link molecular complex control the polymerization of F-actin in the stereocilia. Alternatively, sans might exert a direct role in F-actin polymerization. To address the first possibility, we produced a postnatal conditional knockout of the cadherin-23 gene by crossing $Cdh23^{fl/fl}$ mice (24) with $Myo15\text{-}cre^{+/-}$ mice. In the $Cdh23^{fl/fl}Myo15\text{-}cre^{+/-}$ mice, ABR recordings first showed a hearing impairment at P16. At P22, ABR recordings lacked identifiable waves even at the highest sound intensity (105 dB SPL) for all frequencies tested, thus indicating IHC impairment (Fig. S4*B*). At this stage, we did not detect CM and DPOAEs either, which indicated that the function of OHCs was also severely impaired (Fig. S4 *C* and *D*). Scanning EM performed at P16 and P22 established that IHC and OHC hair bundles had normal shapes and were cohesive. However, both IHC and OHC hair bundles displayed morphological anomalies that were similar to those observed in $Ush1g^{fl/fl}Myo15\text{-}cre^{+/-}$ mice (Fig. S4*E*), specifically, the loss of the prolate shape of stereocilia tips within the medium row and decrease of the length of stereocilia from the small and medium rows, followed by progressive loss of the stereocilia in these rows (Fig. S4*F*). This strongly suggests that the tip-link, which is lost in the absence of cadherin-23, has a positive effect on the size of the stereocilia from these two rows. We conclude that the decrease of stereocilia length that we observed in the *Ush1g* conditional knockout mice is likely to be the consequence of the tip-link loss. We suggest that the size anomalies of the small and medium rows of stereocilia (occurring between P1 and P5), which failed in $Ush1g^{-/-}$ mice (Fig. S3) and also in $Cdh23^{-/-}$ mice and protocadherin-15–deficient mutant mice ($Pcdh15^{av3J/av3J}$) (17), in fact results from the same mechanism. As soon as the tip-link can operate (at P1 in the mouse cochlea), it may play a role in F-actin polymerization in the two smallest rows of stereocilia, a role that, we suggest, is maintained during the continuous steady-state renewal of the stereocilia actin filaments in the mature hair bundle. The presence of the MET machinery may provide the conditions that allow F-actin polymerization to occur in the stereocilia of the two smallest stereocilia rows. Alternatively, the activity of the MET machinery may be directly coupled to the F-actin polymerization. These two hypotheses are not mutually exclusive. The tension exerted by the tip-link on the plasma membrane may be coupled to the kinetics of actin polymerization that takes place at the stereociliary distal end. As a result of these forces, the activity of proteins that promote F-actin elongation and that are sensitive to forces in the piconewton range, such as the formins, may be

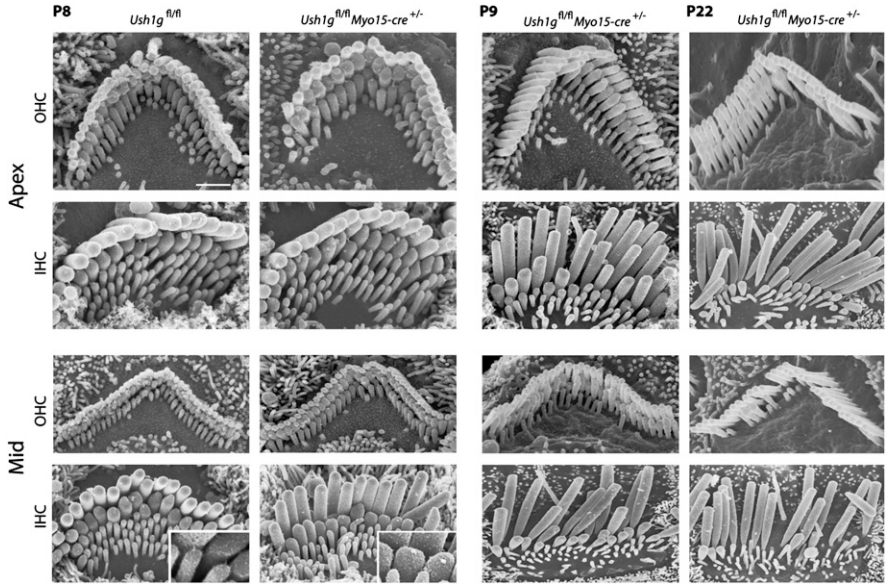

Fig. 2. Hair bundle morphology in OHCs and IHCs from *Ush1g*$^{fl/fl}$*Myo15-cre*$^{+/-}$ P8 mice. Scanning electron microscopy analysis of OHCs and IHCs from the apex (*Upper*) and from the middle region of the cochlea (*Lower*) in *Ush1g*$^{fl/fl}$ and *Ush1g*$^{fl/fl}$*Myo15-cre*$^{+/-}$ P8 mice. In the apical region, the hair bundles of *Ush1g*$^{fl/fl}$*Myo15-cre*$^{+/-}$ IHCs and OHCs are cohesive. In the apical region, the hair bundles of *Ush1g*$^{fl/fl}$*Myo15-cre*$^{+/-}$ IHCs and OHCs are cohesive, the tip-links are present, and prolate-shaped stereocilia tips are systematically observed. In the middle region, no differences were detected between *Ush1g*$^{fl/fl}$ and *Ush1g*$^{fl/fl}$*Myo15-cre*$^{+/-}$ OHCs. In contrast, the presence of nonprolate-shaped stereocilia tips within the middle row of stereocilia was frequently detected in *Ush1g*$^{fl/fl}$*Myo15-cre*$^{+/-}$ IHCs, and the number of tip-links that could be detected in these cells was reduced. At P9, additional hair bundle anomalies appeared in the *Ush1g*$^{fl/fl}$*Myo15-cre*$^{+/-}$ IHCs from the mid to the apex of the cochlea; specifically, some stereocilia within the small and middle rows had reduced heights. No defects were found in OHCs from the cochlear apex at this stage, but in the middle region of the cochlea, we found the same anomalies as in IHCs. At P22, the reduction of the stereocilia length dramatically worsened, and some of the stereocilia from the small row had even disappeared in both IHCs and OHCs. Notably, the size of the stereocilia that compose the tall row was unchanged in *Ush1g*$^{fl/fl}$*Myo15-cre*$^{+/-}$ mutants. (Scale bar: 1 μm.)

modulated (28). Tip-link tension may also enhance actin polymerization by increasing MET channel opening probability, and hence the influx of Ca^{2+} ions at the stereocilia tip may modulate actin polymerization (27). The rapid [in about 2 d, the time period for the renewal of stereociliary actin (29)] and total disappearance/collapse of the small and medium stereocilia rows contrasts with the maintenance of stereocilia of reduced size in mice defective for myosin XV, whirlin, or espin (30, 31) and

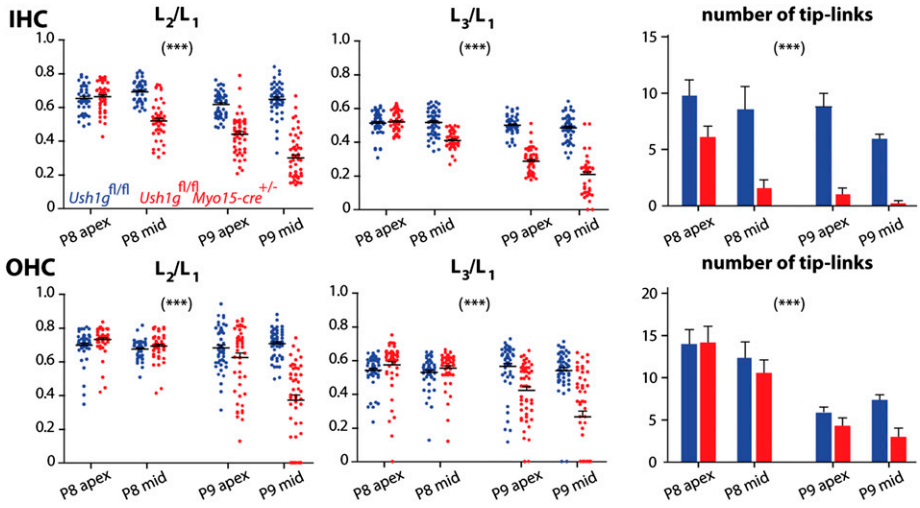

Fig. 3. Analysis of stereocilia length in IHCs and OHCs from P8 and P9 *Ush1g*$^{fl/fl}$*Myo15-cre*$^{+/-}$ mice. Data corresponding to *Ush1g*$^{fl/fl}$ and *Ush1g*$^{fl/fl}$*Myo15-cre*$^{+/-}$ mice are indicated in blue and in red, respectively. Five cells were analyzed in each group. The length of every measurable stereocilium from the middle and small rows was normalized to the mean length of stereocilia in the tall row (L_2/L_1 and L_3/L_1, respectively; mean ± SEM). The numbers (mean ± SEM) of tip-links detected in the apical (apex) and middle (mid) regions of the cochlea are indicated by histograms (*Right* panels). In *Ush1g*$^{fl/fl}$*Myo15-cre*$^{+/-}$ IHCs (*Upper* panels), there is a progressive reduction of the stereocilia length in the middle and small rows and a parallel decrease of the number of tip-links detected, compared with *Ush1g*$^{fl/fl}$ IHCs (two-way ANOVA, $P < 10^{-4}$ for both comparisons). In *Ush1g*$^{fl/fl}$*Myo15-cre*$^{+/-}$ OHCs (*Lower* panels), a decrease of the stereocilia length and number of tip-links is also observed (two-way ANOVA, $P < 10^{-4}$ for both comparisons). In *Ush1g*$^{fl/fl}$*Myo15-cre*$^{+/-}$ P9 mice, note that some stereocilia have completely disappeared in both IHCs and OHCs (red dots on the *x* axis), specifically, 4% of stereocilia from the small row in IHCs of the mid cochlear region, 3% of stereocilia from the small row in OHCs of the apical region, and 15% and 32% of the stereocilia from the middle and small rows in OHCs of the mid region, respectively.

suggests that there is a complete failure of actin polymerization in the absence of the tip-link. The present findings provide experimental results in support of the role proposed for tip-link tension in the control of the stereocilia length (30).

Sans Belongs to the Tip-Link Molecular Complex and Interacts with Protocadherin-15 and Cadherin-23. The anti-sans antibodies described previously (13) were tested on *Ush1g*$^{-/-}$ mice. The labeling observed in the cochlear hair cells from wild-type mice persisted unchanged in the mutant mice, indicating the nonspecificity of these antibodies. We produced another polyclonal antibody directed against the SAM domain of sans (*Materials and Methods*). This antibody labeled the stereocilia in *Ush1g*$^{fl/fl}$, but not in *Ush1g*$^{-/-}$ mice, thereby proving the specificity of the stereocilia labeling (Fig. 4*A*). In the cochlea, sans was detected in the apical region of the hair bundles as early as embryonic day 16.5 (E16.5), and at P1 it was present at the hair bundle tips, as were the other four USH1 proteins (17). We conclude that sans belongs to the USH1 protein network that is required for the cohesion of hair bundles in cochlear hair cells during the early stages of their development. Thereafter, at P8, spots of sans labeling were observed in the apical region of all three stereocilia rows (Fig. 4*C*). Immunogold labeling confirmed the presence of sans at the tip of the small and middle stereocilia rows (Fig. 4*D*). Notably, the labeling of the small and medium rows was always located at the tips of stereocilia. In *Ush1g*$^{fl/fl}$*Myo15-cre*$^{+/-}$ mice at P8, sans labeling was no longer detected in IHCs, but it was still present in OHCs, in accordance with the preservation of their MET currents at this stage (Fig. 4*C*).

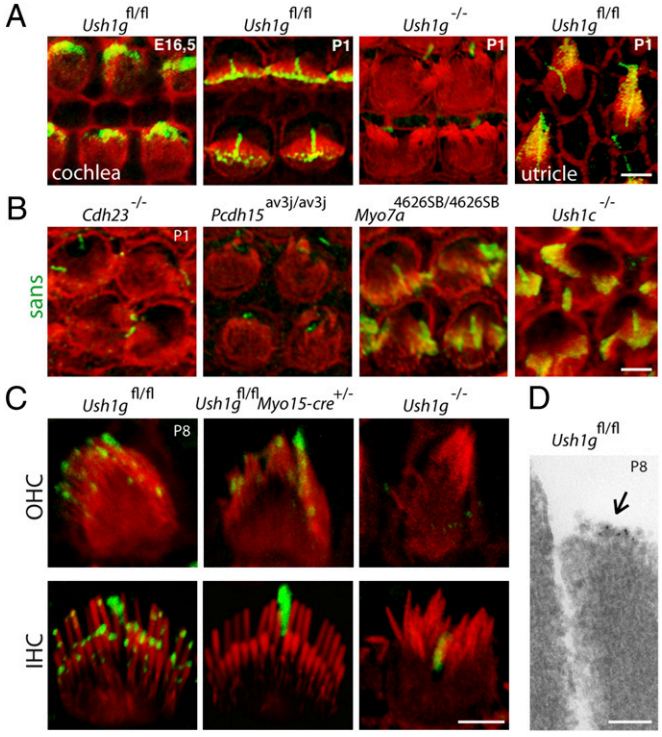

Fig. 4. (*A*) Distribution of sans in mouse cochlear and vestibular hair cells. Hair bundles from E16.5 and P1 mouse cochlear and utricular sensory cells stained using phalloidin to detect F-actin (red) and the antibody to sans (green). From E16.5, sans is detected in the actin-rich protrusions that grow on top of the newly differentiated cochlear hair cells, with a particular concentration at their actin-free distal end. In the P1 cochlea, sans immunoreactivity becomes restricted to stereocilia tips. The stereocilia immunoreactivity is specific to sans as it is absent in *Ush1g*$^{-/-}$ P1 mice. In P1 vestibular hair cells, the sans signal is also restricted to stereocilia tips. (*B*) Distribution of sans in different *Ush1* mutant mice at P1. Hair bundles of sensory cells from the cochlear basal turn of *Cdh23*$^{-/-}$, *Pcdh15*$^{av3J/av3J}$, *Myo7a*$^{4626SB/4626SB}$, and *Ush1c*$^{-/-}$ P1 mice are shown. F-actin (red) and sans (green) stainings as in *A*. Note the absence of immunoreactivity in the hair bundles of *Cdh23*$^{-/-}$ and *Pcdh15*$^{av3J/av3J}$ mice. (*C*) Distribution of sans in cochlear hair cells from P8 *Ush1g*$^{fl/fl}$, *Ush1g*$^{fl/fl}$*Myo15-cre*$^{+/-}$, and *Ush1g*$^{-/-}$ mice. F-actin (red) and sans (green) stainings as in *A*. In OHCs from *Ush1g*$^{fl/fl}$ mice, sans is detected in the apical region of the stereocilia. In IHCs from *Ush1g*$^{fl/fl}$ mice, sans is detected at the distal ends of the stereocilia from the short, medium, and tall rows. Occasional subapical labeling of some tall stereocilia is compatible with a presence of sans at the upper insertion point of the tip-link. In *Ush1g*$^{fl/fl}$ *Myo15-cre*$^{+/-}$ P8 mice, sans is still detected in OHCs, but is no longer present in IHCs. The immunoreactivity of stereocilia is specific as it is absent in *Ush1g*$^{-/-}$ P8 mice. Note the nonspecific immunolabeling of the kinocilium. (*D*) Sans immunogold labeling of a stereocilium from the intermediate stereocilia row in an *Ush1g*$^{fl/fl}$ P8 OHC (shown in a transmission electron micrograph). The gold particles (5-nm gold particles, arrow.) are located at the tip of the stereocilium. (Scale bars: 2 μm in *A*–*C* and 100 nm in *D*.)

In the absence of harmonin (*Ush1c*$^{-/-}$) or myosin VIIa (*Myo7a*$^{4626SB/4626SB}$), sans was properly located at the apical end of the hair bundles in IHCs and OHCs at P1. In contrast, sans could not be detected in *Cdh23*$^{-/-}$ and *Pcdh15*$^{av3J/av3J}$ mutant mice that lack cadherin-23 and protocadherin-15, respectively (Fig. 4*B*). We thus asked whether sans interacts with the cytoplasmic regions of these cadherins. By coexpressing sans with a chimeric cadherin composed of the extracellular region of E-cadherin and the cytoplasmic region of either cadherin-23 or protocadherin-15 (CD1, CD2, or CD3 isoforms; *Materials and Methods*) in transfected COS-7 cells (2), we found that sans is indeed recruited to the plasma membrane when either cadherin-23 or protocadherin-15 (except the CD1 isoform) is present (Fig. S8). In the developing hair bundle, sans is thus likely to be present at both ends of the transient lateral links that are made of cadherin-23 and protocadherin-15. On the basis of the immunodetection of sans in the region of the tip-link lower insertion point in the stereocilia from the small and middle rows at later stages, as well as the interaction, in cotransfected cells, between sans and the CD3 isoform of protocadherin-15 that is believed to form the lower part of the tip-link (8, 32), we conclude that sans belongs to the molecular complex present at the lower insertion point of the tip-link. However, we cannot exclude the possibility that sans also belongs to the molecular complex associated with the upper insertion point of the tip-link because the protein was also detected on the lateral side of some stereocilia in the taller row (Fig. 4) and was recruited to the plasma membrane by cadherin-23 in cotransfected cells (Fig. S8). Notably, the disappearance of the tip-links that we observed in IHCs from *Ush1g*$^{fl/fl}$*Myo15-cre*$^{+/-}$ P8 mice fully accounts for the decrease of the MET current amplitude in these cells. The less-than-1-d delay between the time when sans becomes undetectable and the time when tip-links disappear and the MET current decreases suggests that sans is involved in either the maintenance of the tip-link or its renewal.

Materials and Methods

Experiments on mice were carried out according to Institut National de la Santé et de la Recherche Médicale and Institut Pasteur welfare guidelines.

Whole-Mount Immunofluorescence. Rabbit antisera were raised against recombinant proteins encompassing the SAM domain (aa 369–455) of sans (GenBank accession no. NM_176847), and intracellular fragments of the protocadherin-15 CD1 (aa 1612–1726; GenBank accession no. Q99PJ1), CD2 (aa 1652–1790; GenBank accession no. Q0ZM28), or CD3 (aa 1522–1682; GenBank accession no. Q0ZM20) isoforms. Antibodies were affinity-purified against the corresponding antigens coupled to an NHS column (GE Healthcare). We used the N1 polyclonal antibody to detect cadherin-23 (3).

Expression Vectors. A recombinant pCMV vector encoding sans and recombinant pcDNA3 vectors encoding the extracellular and transmembrane domains of human E-cadherin fused to the cytoplasmic domain of either human cadherin-23 lacking the alternative exon 68-encoded fragment (GenBank

accession no. NP_001165405) or mouse protocadherin-15 (CD1, CD2, and CD3 isoforms; GenBank accession nos. NM_001142740, HQ420254, and HQ404375, respectively) were engineered for expression in COS-7 cells (2).

Scanning Electron Microscopy. Mouse inner ears were processed with osmium tetroxide/thiocarbohydrazide method as previously described (33). Samples were analyzed by field emission scanning electron microscopy operated at 5 kV (Jeol JSM6700F).

Immunogold Labeling. For transmission electron microscopy, gold-labeled tissues were washed, refixed in 2.5% glutaraldehyde in 0.1 M cacodylate buffer pH 7.2 containing 1% tannic acid, washed in buffer, and postfixed in 1% osmium tetroxide as previously described (32).

In Vivo and in Vitro Electrophysiological Recordings and Data Analysis. ABRs, CM, and DPOAEs were recorded in anesthetized mice and analyzed as described previously (34, 35).

Electrophysiological cell recordings were performed on cochlear and utricular explants from mice aged between P1 and P8 (cochlear hair cells, n = 286; vestibular hair cells, n = 54), as reported (22). The probe used for mechanical stimulation of the hair bundles was secured to a stack-type piezoelectric actuator (PA8/12; Piezosystem Jenas) driven by a low-voltage power supply (30V300, Piezosystem Jena). As measured offline with a displacement monitor containing photodiodes, the first two milliseconds of the time course of probe motion were well described by an exponential rise with a time constant of 100 μs (22). Data were analyzed in Matlab, version 7.0 (MathWorks). $P_o(X)$ curves were fitted with a three-state Boltzmann relation (22). For sensitivity measurements, the mean value of the three-state Boltzmann relation derivative was calculated for displacements corresponding to P_0 values between 0.2 and 0.8.

Statistical Analysis. Statistical significance was tested by using either two-way analysis of variance (two-way ANOVA) coupled to the Bonferroni posttest or two-tailed unpaired t test with Welch's correction using Prism software (GraphPad). Statistical significances are indicated on the figures (Figs. 1 and 3 and Figs. S2–S7); the designations (ns), (*), (**), and (***) correspond to nonsignificant ($P > 0.05$), $P < 0.05$, $P < 0.01$, and $P < 0.001$, respectively.

ACKNOWLEDGMENTS. We thank Jacqueline Levilliers for her help in the preparation of the manuscript and Sylvie Nouaille for technical help. We are grateful to the Institut Clinique de la Souris (Illkirch, France) for engineering *Ush1g* and *Cdh23* recombinant mice. This work was supported by FAUN Stiftung (Suchert Foundation), Fondation Raymonde and Guy Strittmatter, LHW-Stiftung, the Conny Maeva Charitable Foundation, Fondation Orange, and the Louis-Jeantet Foundation. R.J.G. and G.P.R. are supported by The Wellcome Trust.

1. Petit C, Richardson GP (2009) Linking genes underlying deafness to hair-bundle development and function. *Nat Neurosci* 12:703–710.
2. Boëda B, et al. (2002) Myosin VIIa, harmonin and cadherin 23, three Usher I gene products that cooperate to shape the sensory hair cell bundle. *EMBO J* 21:6689–6699.
3. Michel V, et al. (2005) Cadherin 23 is a component of the transient lateral links in the developing hair bundles of cochlear sensory cells. *Dev Biol* 280:281–294.
4. El-Amraoui A, Petit C (2005) Usher I syndrome: Unravelling the mechanisms that underlie the cohesion of the growing hair bundle in inner ear sensory cells. *J Cell Sci* 118:4593–4603.
5. Pickles JO, Comis SD, Osborne MP (1984) Cross-links between stereocilia in the guinea pig organ of Corti, and their possible relation to sensory transduction. *Hear Res* 15: 103–112.
6. Furness DN, Hackney CM (1985) Cross-links between stereocilia in the guinea pig cochlea. *Hear Res* 18:177–188.
7. Siemens J, et al. (2004) Cadherin 23 is a component of the tip link in hair-cell stereocilia. *Nature* 428:950–955.
8. Ahmed ZM, et al. (2006) The tip-link antigen, a protein associated with the transduction complex of sensory hair cells, is protocadherin-15. *J Neurosci* 26:7022–7034.
9. Kazmierczak P, et al. (2007) Cadherin 23 and protocadherin 15 interact to form tip-link filaments in sensory hair cells. *Nature* 449:87–91.
10. Hudspeth AJ (2005) How the ear's works work: Mechanoelectrical transduction and amplification by hair cells. *C R Biol* 328:155–162.
11. Beurg M, Fettiplace R, Nam JH, Ricci AJ (2009) Localization of inner hair cell mechanotransducer channels using high-speed calcium imaging. *Nat Neurosci* 12: 553–558.
12. Siemens J, et al. (2002) The Usher syndrome proteins cadherin 23 and harmonin form a complex by means of PDZ-domain interactions. *Proc Natl Acad Sci USA* 99: 14946–14951.
13. Adato A, et al. (2005) Interactions in the network of Usher syndrome type 1 proteins. *Hum Mol Genet* 14:347–356.
14. Senften M, et al. (2006) Physical and functional interaction between protocadherin 15 and myosin VIIa in mechanosensory hair cells. *J Neurosci* 26:2060–2071.
15. Pan L, Yan J, Wu L, Zhang M (2009) Assembling stable hair cell tip link complex via multidentate interactions between harmonin and cadherin 23. *Proc Natl Acad Sci USA* 106:5575–5580.
16. Bahloul A, et al. (2010) Cadherin-23, myosin VIIa and harmonin, encoded by Usher syndrome type I genes, form a ternary complex and interact with membrane phospholipids. *Hum Mol Genet* 19:3557–3565.
17. Lefèvre G, et al. (2008) A core cochlear phenotype in USH1 mouse mutants implicates fibrous links of the hair bundle in its cohesion, orientation and differential growth. *Development* 135:1427–1437.
18. Yan J, Pan L, Chen X, Wu L, Zhang M (2010) The structure of the harmonin/sans complex reveals an unexpected interaction mode of the two Usher syndrome proteins. *Proc Natl Acad Sci USA* 107:4040–4045.
19. Kikkawa Y, et al. (2003) Mutations in a new scaffold protein Sans cause deafness in Jackson shaker mice. *Hum Mol Genet* 12:453–461.
20. Lallemand Y, Luria V, Haffner-Krausz R, Lonai P (1998) Maternally expressed PGK-Cre transgene as a tool for early and uniform activation of the Cre site-specific recombinase. *Transgenic Res* 7:105–112.
21. Lelli A, Asai Y, Forge A, Holt JR, Géléoc GS (2009) Tonotopic gradient in the developmental acquisition of sensory transduction in outer hair cells of the mouse cochlea. *J Neurophysiol* 101:2961–2973.
22. Michalski N, et al. (2009) Harmonin-b, an actin-binding scaffold protein, is involved in the adaptation of mechanoelectrical transduction by sensory hair cells. *Pflugers Arch* 459:115–130.
23. Waguespack J, Salles FT, Kachar B, Ricci AJ (2007) Stepwise morphological and functional maturation of mechanotransduction in rat outer hair cells. *J Neurosci* 27: 13890–13902.
24. Etournay R, et al. (2010) Cochlear outer hair cells undergo an apical circumference remodeling constrained by the hair bundle shape. *Development* 137:1373–1383.
25. Dallos P, Harris D (1978) Properties of auditory nerve responses in absence of outer hair cells. *J Neurophysiol* 41:365–383.
26. Steel KP, Harvisty R (1996) Assessing hearing, vision and balance in mice. *What's Wrong With My Mouse? New Interplays Between Mouse Genes and Behavior* (Society for Neuroscience, Washington, DC), pp 26–38.
27. Tilney LG, Tilney MS, Cotanche DA (1988) Actin filaments, stereocilia, and hair cells of the bird cochlea. V. How the staircase pattern of stereociliary lengths is generated. *J Cell Biol* 106:355–365.
28. Bershadsky A, Kozlov M, Geiger B (2006) Adhesion-mediated mechanosensitivity: A time to experiment, and a time to theorize. *Curr Opin Cell Biol* 18:472–481.
29. Schneider ME, Belyantseva IA, Azevedo RB, Kachar B (2002) Rapid renewal of auditory hair bundles. *Nature* 418:837–838.
30. Manor U, Kachar B (2008) Dynamic length regulation of sensory stereocilia. *Semin Cell Dev Biol* 19:502–510.
31. Gillespie PG, Müller U (2009) Mechanotransduction by hair cells: Models, molecules, and mechanisms. *Cell* 139:33–44.
32. Goodyear RJ, Forge A, Legan PK, Richardson GP (2010) Asymmetric distribution of cadherin 23 and protocadherin 15 in the kinocilial links of avian sensory hair cells. *J Comp Neurol* 518:4288–4297.
33. Furness DN, Katori Y, Nirmal Kumar B, Hackney CM (2008) The dimensions and structural attachments of tip links in mammalian cochlear hair cells and the effects of exposure to different levels of extracellular calcium. *Neuroscience* 154:10–21.
34. Le Calvez S, Avan P, Gilain L, Romand R (1998) CD1 hearing-impaired mice. I: Distortion product otoacoustic emission levels, cochlear function and morphology. *Hear Res* 120:37–50.
35. Verpy E, et al. (2008) Stereocilin-deficient mice reveal the origin of cochlear waveform distortions. *Nature* 456:255–258.

Supporting Information

Caberlotto et al. 10.1073/pnas.1017114108

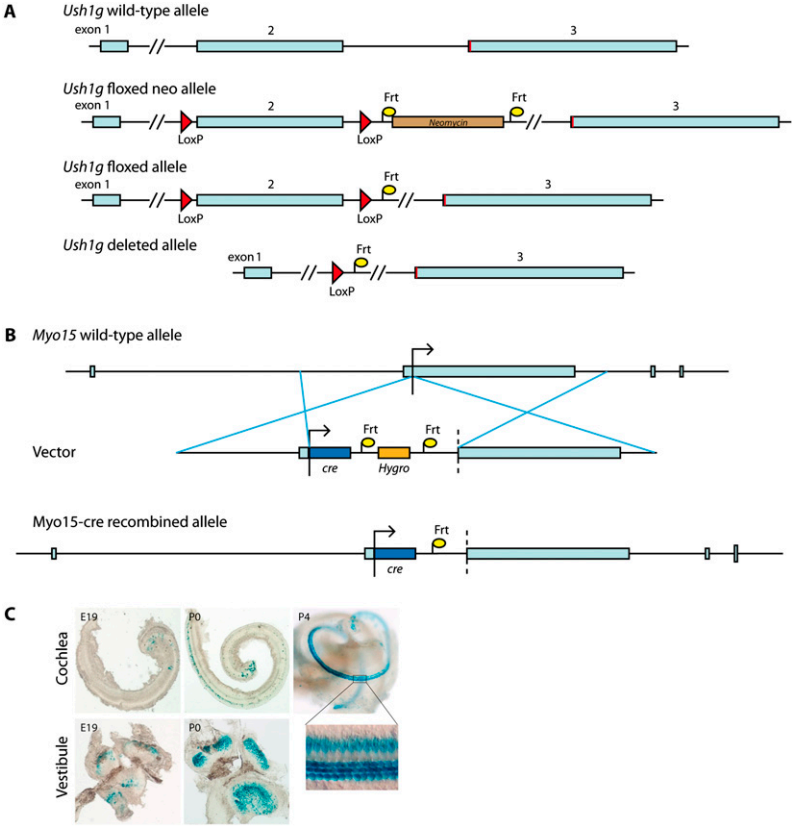

Fig. S1. Engineering of *Ush1g* knockout mice and *Myo15-cre* mice. (*A*) Schematic of the recombinant *Ush1g* alleles. A targeting vector was designed in which *loxP* sites were introduced upstream and downstream of *Ush1g* exon 2, and a neo cassette flanked with *FRT* sites as selectable marker was introduced downstream of exon 2. The targeting construct was electroporated into embryonic stem cells from the 129S1/SvImJ mouse strain, and positive ES cells were selected by their resistance to G418. Stem cells carrying the targeted construct were injected into blastocysts from C57BL/6J mice to obtain chimeric mice. After germline transmission, mice were crossed with C57BL/6J mice producing Flp recombinase to remove the neo cassette. The $Ush1g^{fl/fl}$ mice (MGI:4361359) lack the neo cassette and behave like wild-type ($^{+/+}$) mice. $Ush1g^{fl/fl}$ mice were crossed either with the PGK-Cre^{m} transgenic mouse strain carrying the cre recombinase gene driven by the early acting phosphoglycerate kinase-1 gene promoter or with *Myo15-cre* recombinant mice carrying the cre recombinase gene driven by the myosin-15 gene promoter which, in the inner ear, deletes only the floxed fragment in hair cells. Genotyping of *Ush1g* recombinant animals was carried out by means of two PCR amplifications, using either *oligo-3* (5′-GTCAAAGGATCAGATCACTCGCAG-3′) and *oligo-1* (5′-GGGAGTCGGCTTAACACCACATTG-3′) to detect the wild-type (323-bp amplicon) or floxed (423-bp amplicon) alleles or *oligo-3* and *oligo-4* (5′-CAGTTTCCCCATGTTGATCACCAAC-3′) to detect the presence of a deleted allele lacking *Ush1g* exon 2 (322-bp amplicon). All studies were performed on mixed C57BL/6–129/Sv genetic backgrounds. (*B*) Schematic of the *Myo15-Cre* allele engineered for this study. The cre recombinase gene was placed under the control of the *Myo15* promoter: a targeting construct was designed containing a hygromycin resistance cassette flanked with *FRT* sites and introduced in C57BL/6J mice blastocysts, and after germline transmission, mice were crossed with C57BL/6J mice producing Flp recombinase to remove the hygromycin cassette (MGI:4361284). The heterozygote $Myo15\text{-}cre^{+/-}$ mice behave like wild-type ($^{+/+}$) mice. Genotyping of the animals was done using *Myo15-F* primer (5′-AGGGACCTGACTCCACTTTGGG-3′) with either *Myo15-R* primer (5′-GGAACTGACCTTTCTTAGAGATCTTGGG-3′) to detect the wild-type allele or *cre-R* (5′-TGGTGCACAGTCAGCAGGTTGG-3′) to detect the *Myo15-cre* allele (450-bp amplicon). (*C*) X-Gal staining on $ROSA26^{+/-}Myo15\text{-}cre^{+/-}$ mice. The temporal-spatial expression pattern of *cre* driven by the *Myo15* promoter in the inner ear was assessed by crossing $Myo15\text{-}cre^{+/-}$ mice with ROSA26-lacZ reporter mice (1). The cre-driven *lacZ* expression was studied in the inner ear of $ROSA26^{+/-}Myo15\text{-}cre^{+/-}$ mice using X-Gal histochemistry. *LacZ* expression was first detected in vestibular hair cells at E19, and in hair cells from the cochlear base at P0. At P4, *lacZ* expression was detected in all cochlear hair cells.

1. Soriano P (1999) Generalized lacZ expression with the ROSA26 Cre reporter strain. *Nat Genet* 21:70–71.

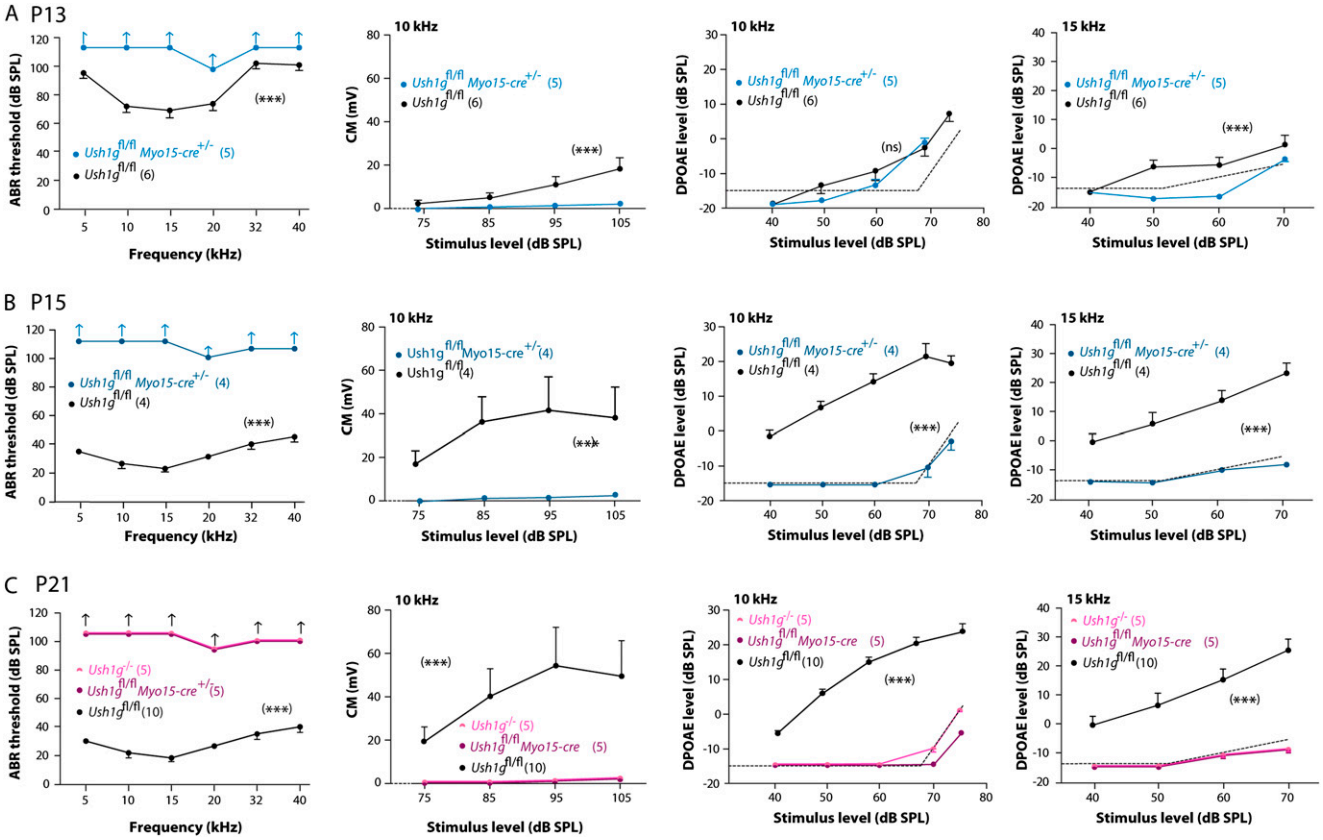

Fig. S2. Analysis of the auditory function in *Ush1g*$^{fl/fl}$*Myo15-cre*$^{+/-}$ P13, P15, and P21 mice and in *Ush1g*$^{-/-}$ P21 mice. (*A*, first graph) Auditory brainstem response (ABR) thresholds (mean ± SEM) in *Ush1g*$^{fl/fl}$ (black line) and *Ush1g*$^{fl/fl}$*Myo15-cre*$^{+/-}$ (blue line) P13 mice for 5- to 40-kHz tone bursts. *Ush1g*$^{fl/fl}$*Myo15-cre*$^{+/-}$ mutants show a total absence of evoked response (two-way ANOVA, $P < 10^{-3}$). (second graph) Growth functions of cochlear microphonics (CM) (mean ± SEM) at increasing stimulus level from 75 to 105 dB for *Ush1g*$^{fl/fl}$ mice and from 90 to 100 dB for *Ush1g*$^{fl/fl}$*Myo15-cre*$^{+/-}$ mice. (third and fourth graphs) DPOAE amplitude (mean ± SEM) at frequency $2f_1 - f_2$ for f_2 = 10 kHz and f_2 = 15 kHz in *Ush1g*$^{fl/fl}$ and *Ush1g*$^{fl/fl}$*Myo15-cre*$^{+/-}$ P13 mice. The DPOAE amplitude was recorded in response to two equal-level primary tones, f_1 and f_2, with f_2/f_1 = 1.20. Cubic DPOAEs were elicited by a CubeDis system (Mimosa Acoustics, v2.43). Frequency f_2 was swept at one-tenth-octave steps from 4 to 20 kHz (levels increased stepwise from 30 to 70 dB SPL). For f_2 = 10 kHz, *Ush1g*$^{fl/fl}$*Myo15-cre*$^{+/-}$ mice show detectable DPOAEs for stimulus level from 60 to 70 dB, whereas no DPOAEs are detected for f_2 = 15 kHz. (*B*, first graph) ABR thresholds (mean ± SEM) in *Ush1g*$^{fl/fl}$ (black line) and *Ush1g*$^{fl/fl}$*Myo15-cre*$^{+/-}$ (blue line) P15 mice for 5- to 40-kHz tone bursts. *Ush1g*$^{fl/fl}$*Myo15-cre*$^{+/-}$ mutants show a total absence of evoked response (two-way ANOVA, $P < 10^{-3}$). (second graph) Growth functions of CM (mean ± SEM) at an increasing stimulus level from 75 to 105 dB for *Ush1g*$^{fl/fl}$ mice and from 90 to 100 dB for *Ush1g*$^{fl/fl}$*Myo15-cre*$^{+/-}$ mice. (third and fourth graphs) DPOAE amplitude (mean ± SEM) at frequency $2f_1 - f_2$ (f_1/f_2 = 1.20) for f_2 = 10 kHz and f_2 = 15 kHz in *Ush1g*$^{fl/fl}$ and *Ush1g*$^{fl/fl}$*Myo15-cre*$^{+/-}$ P15 mice. *Ush1g*$^{fl/fl}$*Myo15-cre*$^{+/-}$ mice have no detectable DPOAEs. (*C*, first graph) ABR thresholds (mean ± SEM) in *Ush1g*$^{fl/fl}$ (black lines), *Ush1g*$^{-/-}$ (pink line), and *Ush1g*$^{fl/fl}$*Myo15-cre*$^{+/-}$ (purple line) P21 mice for 5- to 40-kHz tone bursts. *Ush1g*$^{-/-}$ and *Ush1g*$^{fl/fl}$*Myo15-cre*$^{+/-}$ mutants show a total absence of evoked response (two-way ANOVA, $P < 10^{-3}$). (second graph) Growth functions of CM (mean ± SEM at an increasing stimulus level from 75 to 105 dB. (third and fourth graphs) DPOAE amplitude (mean ± SEM) at frequency $2f_1 - f_2$ (f_1/f_2 = 1.20) in *Ush1g*$^{fl/fl}$, *Ush1g*$^{-/-}$, and *Ush1g*$^{fl/fl}$*Myo15-cre*$^{+/-}$ P21 mice. *Ush1g*$^{-/-}$ and *Ush1g*$^{fl/fl}$*Myo15-cre*$^{+/-}$ mice have no detectable DPOAEs. Dashed line represents noise floor below 65 dB SPL and instrumental distortion above 65 dB SPL.

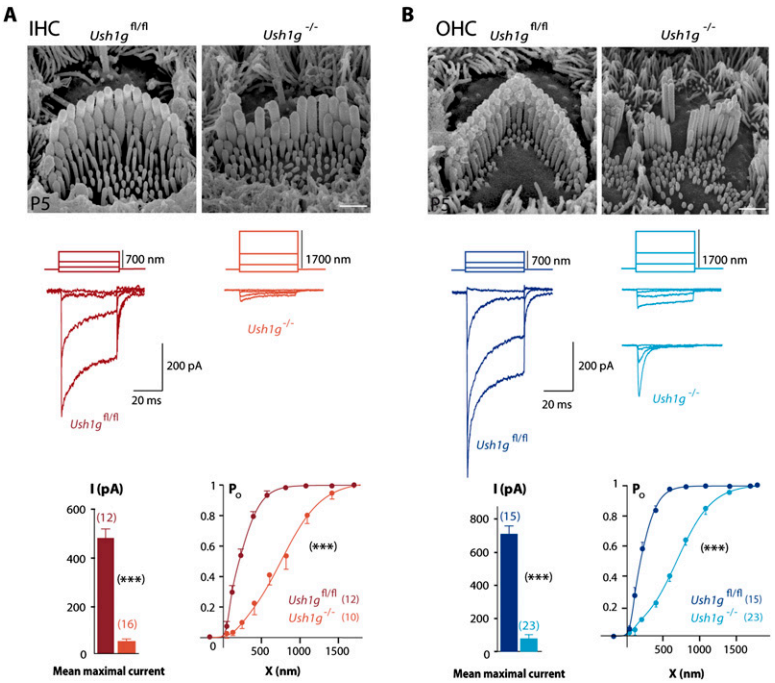

Fig. S3. Hair cell morphology and mechanoelectrical transduction current recordings in inner hair cells (IHCs) and outer hair cells (OHCs) from *Ush1g*$^{-/-}$ P5 mice. (*A*, *Top*) scanning electron microscopy analysis of IHCs from *Ush1g*$^{fl/fl}$ and *Ush1g*$^{-/-}$ P5 mice. (Scale bar: 1 μm.) In *Ush1g*$^{-/-}$ IHCs, some stereocilia of the second row (about 10%) have a prolate end shape, which suggests that some tip-links are still present. Note the reduced length of most stereocilia from the small and medium rows. (*Middle*) Examples of transduction current recordings in an *Ush1g*$^{fl/fl}$ IHC (*Left* panel in dark-red) and an *Ush1g*$^{-/-}$ IHC from P5 mice while applying different displacement steps with a glass probe in the excitatory direction and a 150-nm step in the inhibitory direction (calibrated voltage command of the stimulator at the top). (*Bottom*) Mean maximum transduction currents and $P_o(X)$ curves plotted for *Ush1g*$^{fl/fl}$ and *Ush1g*$^{-/-}$ P5 mice. The maximal amplitudes of the transduction current are 51 ± 9 pA and 471 ± 40 pA in *Ush1g*$^{-/-}$ and *Ush1g*$^{fl/fl}$ IHCs, respectively (unpaired *t* test, $P < 10^{-4}$). The averaged sensitivity of the transduction currents to hair bundle displacement in the mutant IHCs is 0.99 ± 0.09 μm^{-1} and 2.80 ± 0.15 μm^{-1} in *Ush1g*$^{-/-}$ and *Ush1g*$^{fl/fl}$ IHCs, respectively (unpaired *t* test, $P < 10^{-4}$). $X_{0.5}$ is 745 ± 59 nm and 217 ± 20 nm in *Ush1g*$^{-/-}$ and *Ush1g*$^{fl/fl}$ IHCs, respectively (unpaired *t* test, $P < 10^{-3}$). (*B*, *Top*) Scanning electron microscopy analysis of OHCs from *Ush1g*$^{fl/fl}$ and *Ush1g*$^{-/-}$ P5 mice. Note the fragmented aspect of the hair bundles and the reduced length of most stereocilia from the small and medium rows. However, one can recognize the stereocilia of the first row and some stereocilia of the second row. (Scale bar: 1 μm.) (*Middle*) Examples of transduction current recordings in a *Ush1g*$^{fl/fl}$ OHC and two *Ush1g*$^{-/-}$ OHCs from P5 mice. (*Bottom*) Mean maximum transduction currents and $P_o(X)$ curves plotted for *Ush1g*$^{fl/fl}$ and *Ush1g*$^{-/-}$ P5 mice. The maximal amplitudes of the transduction current are 91 ± 24 pA and 696 ± 50 pA in *Ush1g*$^{-/-}$ and *Ush1g*$^{fl/fl}$ OHCs, respectively (unpaired *t* test, $P < 10^{-3}$). The averaged sensitivity values are 1.51 ± 0.24 μm^{-1} and 2.85 ± 0.26 μm^{-1} in *Ush1g*$^{-/-}$ and *Ush1g*$^{fl/fl}$ OHCs, respectively (unpaired *t* test, $P < 10^{-4}$). In addition, $X_{0.5}$ is 765 ± 63 nm and 202 ± 17 nm in *Ush1g*$^{-/-}$ and *Ush1g*$^{fl/fl}$ OHCs, respectively (unpaired *t* test, $P < 10^{-4}$).

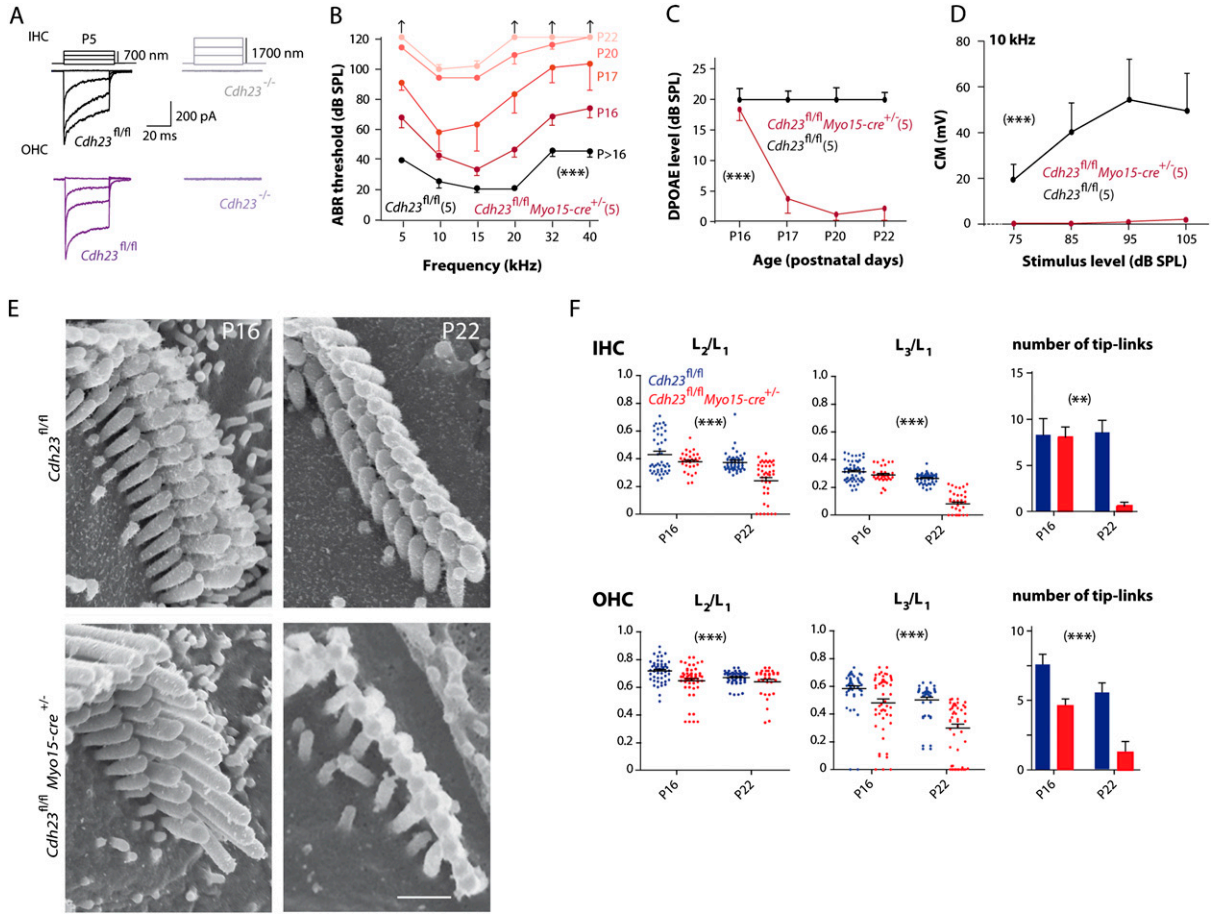

Fig. S4. (*A*) Mechanoelectrical transduction current recordings in inner hair cells (IHCs) and outer hair cells (OHCs) from *Cdh23*$^{fl/fl}$ and *Cdh23*$^{-/-}$ P5 mice. Examples of transduction currents in IHCs (*Upper*) and OHCs (*Lower*) from *Cdh23*$^{fl/fl}$ and *Cdh23*$^{-/-}$ P5 mice in response to a 40-ms mechanical stimulation of the hair bundle. No current is recorded in the *Cdh23*$^{-/-}$ IHC (gray) and OHC (light purple). (*B–D*) Analysis of the auditory function in *Cdh23*$^{fl/fl}$*Myo15-cre*$^{+/-}$ mice at P16, P17, P20, and P22. (*B*) Auditory brainstem response (ABR) thresholds in *Cdh23*$^{fl/fl}$ (black lines) and *Cdh23*$^{fl/fl}$*Myo15-cre*$^{+/-}$ (red lines) P16–P22 mice for 5- to 40-kHz tone bursts (mean ± SEM). *Cdh23*$^{fl/fl}$*Myo15-cre*$^{+/-}$ mutants show progressive hearing loss from P16 to P22 and have profound hearing impairment at P22 (two-way ANOVA, $P < 10^{-4}$). (*C*) Amplitude of the distortion-product otoacoustic emissions (DPOAE) (mean ± SEM) recorded at frequency $2f_1 - f_2$ for a 60-dB SPL two-tone stimulus ($f_1/f_2 = 1.20$) in *Cdh23*$^{fl/fl}$ and *Cdh23*$^{fl/fl}$*Myo15-cre*$^{+/-}$ P16, P17, P20, and P22 mice. *Cdh23*$^{fl/fl}$*Myo15-cre*$^{+/-}$ mice have no detectable DPOAE at P22. (*D*) Growth functions of cochlear microphonics (CM) (mean ± SEM) at an increasing stimulus level from 75 to 105 dB in *Cdh23*$^{fl/fl}$ and *Cdh23*$^{fl/fl}$*Myo15-cre*$^{+/-}$ P22 mice. (*E*) Hair bundle morphology in *Cdh23*$^{fl/fl}$*Myo15-cre*$^{+/-}$ OHCs. Scanning electron microscopy analysis of OHCs in the mid region of the cochlea from *Cdh23*$^{fl/fl}$ (*Upper*) and *Cdh23*$^{fl/fl}$*Myo15-cre*$^{+/-}$ (*Lower*) P16 and P22 mice. At P16, the hair bundles of *Cdh23*$^{fl/fl}$*Myo15-cre*$^{+/-}$ OHCs are cohesive, but some stereocilia of the small row already have reduced heights. At P22, the reduction of the stereocilia length has dramatically worsened in the small and middle rows, and some of the stereocilia from the small row have even disappeared. Notably, the length of the stereocilia in the tall row is unchanged. (Scale bar: 1 μm.) (*F*) Analysis of stereocilia length in IHCs and OHCs from P16 and P22 *Cdh23*$^{fl/fl}$*Myo15-cre*$^{+/-}$ mice. Data corresponding to *Cdh23*$^{fl/fl}$ and *Cdh23*$^{fl/fl}$*Myo15-cre*$^{+/-}$ mice are indicated in blue and in red, respectively. Five cells were analyzed in each group. The length of every measurable stereocilium from the middle and small rows was normalized to the mean length of stereocilia in the tall row (L_2/L_1 and L_3/L_1, respectively; mean ± SEM). The numbers (mean ± SEM) of tip-links detected are indicated by histograms (*Right* panels). In both *Cdh23*$^{fl/fl}$*Myo15-cre*$^{+/-}$ IHCs (*Upper* panels) and OHCs (*Lower* panels), there is a progressive reduction of the stereocilia length and a parallel decrease of the number of tip-links detected, compared with *Cdh23*$^{fl/fl}$ IHCs and OHCs (two-way ANOVA, $P < 10^{-2}$ for all comparisons). In *Cdh23*$^{fl/fl}$*Myo15-cre*$^{+/-}$ P22 mice, note that some stereocilia have completely disappeared in both IHCs and OHCs (red dots on the *x* axis), specifically, 18% of stereocilia from the middle row, 36% from the small row in IHCs, and 32% of stereocilia from the small row in OHCs.

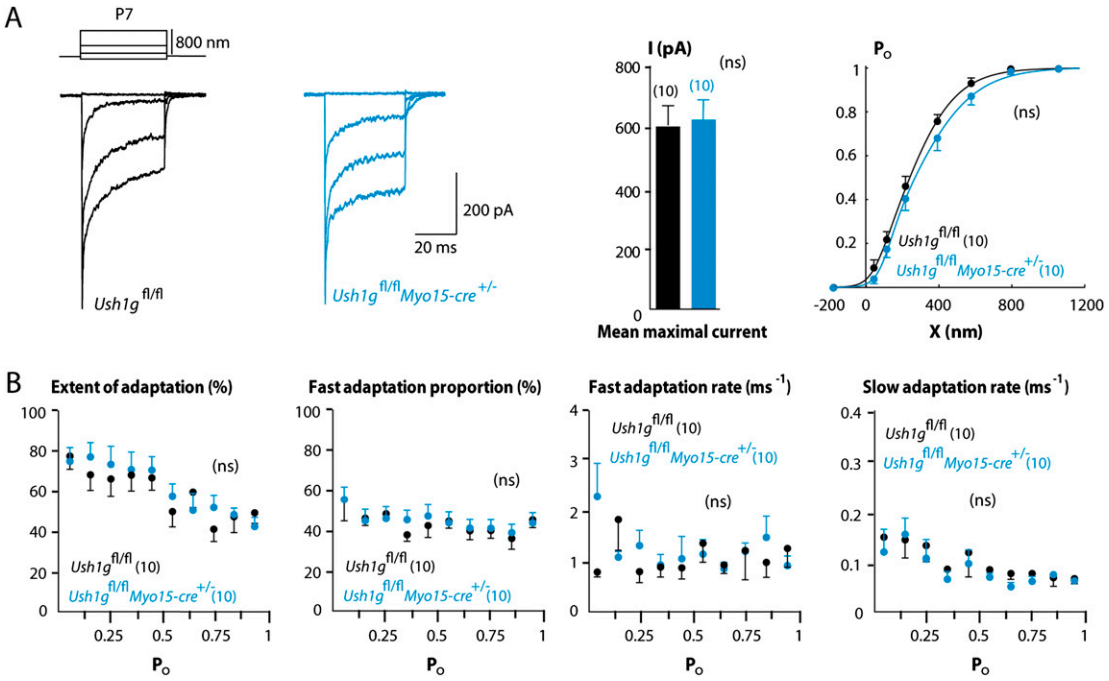

Fig. S5. Analysis of mechanoelectrical transduction current adaptation in inner hair cells (IHCs) from *Ush1g*$^{fl/fl}$*Myo15-cre*$^{+/-}$ P7 mice. Mechanoelectrical transduction currents in cochlear hair cells from the region that is ~40% of the total length of the cochlea from the apex. (*A*) Examples of transduction currents in midcochlear IHCs from *Ush1g*$^{fl/fl}$ (black) and *Ush1g*$^{fl/fl}$*Myo15-cre*$^{+/-}$ (blue) P7 mice. Mean maximum current amplitude is 616 ± 67 pA and 664 ± 71 pA for *Ush1g*$^{fl/fl}$ and *Ush1g*$^{fl/fl}$*Myo15-cre*$^{+/-}$ IHCs, respectively (unpaired *t* test, $P = 0.63$). The $P_o(X)$ curves can be superimposed with values of averaged sensitivity 2.03 ± 0.10 μm^{-1} and 1.85 ± 0.14 μm^{-1} for *Ush1g*$^{fl/fl}$ and *Ush1g*$^{fl/fl}$*Myo15-cre*$^{+/-}$, respectively (unpaired *t* test, $P = 0.35$). In addition, no change in $X_{0.5}$ could be detected in the mutant IHCs with values 248 ± 23 nm and 273 ± 34 nm in *Ush1g*$^{fl/fl}$ and *Ush1g*$^{fl/fl}$*Myo15-cre*$^{+/-}$, respectively (unpaired *t* test, $P = 0.55$). (*B*) We characterized the adaptation in *Ush1g*$^{fl/fl}$ and *Ush1g*$^{fl/fl}$*Myo15-cre*$^{+/-}$ IHCs in terms of its extent and kinetics. The adaptive decline of the transduction current *I* as a function of time *t* was fitted by the double exponential relation $I(t) = A_F\{exp(-(t - t_0)/\tau_F)\} + A_S\{exp(-(t - t_0)/\tau_S)\} + A_{SS}$. In this equation, t_0 is the time at which the stimulus was applied, the fast and slow components of adaptation are characterized by their magnitudes, A_F and A_S, and time constants, τ_F and τ_S, respectively, and A_{SS} describes the transduction current at steady state. From the fit, we deduced the fast and slow adaptation rates, $1/\tau_F$ and $1/\tau_S$, and the proportions, $A_F/(A_F + A_S)$ and $A_S/(A_F + A_S)$, respectively, as well as the extent of adaptation $1 - A_{SS}/(A_F + A_S + A_{SS})$ (1). Statistical significance was tested by using either two-way analysis of variance coupled to the Bonferroni posttest (two-way ANOVA) or two-tailed unpaired *t* test with Welch's correction using the Prism software (GraphPad). We compared the extent of adaptation, the fast adaptation proportion, and the fast and slow adaptation rates in *Ush1g*$^{fl/fl}$ and *Ush1g*$^{fl/fl}$*Myo15-cre*$^{+/-}$ mice, and no change could be detected in the mutant IHCs (two-way ANOVA, $P = 0.34$, $P = 0.60$, $P = 0.42$, and $P = 0.17$, respectively).

1. Kennedy HJ, Evans MG, Crawford AC, Fettiplace R (2003) Fast adaptation of mechanoelectrical transducer channels in mammalian cochlear hair cells. *Nat Neurosci* 6:832–836.

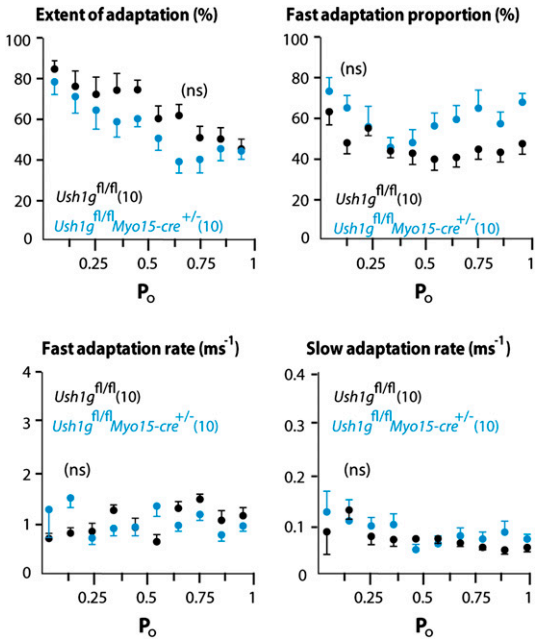

Fig. S6. Analysis of mechanoelectrical transduction current adaptation in *Ush1g*$^{fl/fl}$*Myo15-cre*$^{+/-}$ inner hair cells (IHCs) from the apex. We characterized the adaptation in *Ush1g*$^{fl/fl}$ and *Ush1g*$^{fl/fl}$*Myo15-cre*$^{+/-}$ IHCs from the cochlear apex in terms of its extent and kinetics. The adaptive decline of the transduction current I as a function of time t was fitted by the double exponential relation $I(t) = A_F\{exp(-(t - t_0)/\tau_F)\} + A_S\{exp(-(t - t_0)/\tau_S)\} + A_{SS}$. In this equation, t_0 is the time at which the stimulus was applied; the fast and slow components of adaptation are characterized by their magnitudes, A_F and A_S, and time constants, τ_F and τ_S, respectively; and A_{SS} describes the transduction current at steady state. From the fit, we deduced the fast and slow adaptation rates, $1/\tau_F$ and $1/\tau_S$, and the proportions, $A_F/(A_F + A_S)$ and $A_S/(A_F + A_S)$, respectively, as well as the extent of adaptation $1 - A_{SS}/(A_F + A_S + A_{SS})$ (1). Statistical significance was tested by using either two-way analysis of variance coupled to the Bonferroni posttest (two-way ANOVA) or two-tailed unpaired t test with Welch's correction using the Prism software (GraphPad). We compared the extent of adaptation, the fast adaptation proportion, and the fast and slow adaptation rates in *Ush1g*$^{fl/fl}$ and *Ush1g*$^{fl/fl}$*Myo15-cre*$^{+/-}$ mice, and no change could be detected in the mutant IHCs (two-way ANOVA, $P = 0.78$, $P = 0.44$, $P = 0.08$, and $P = 0.16$, respectively).

1. Kennedy HJ, Evans MG, Crawford AC, Fettiplace R (2003) Fast adaptation of mechanoelectrical transducer channels in mammalian cochlear hair cells. *Nat Neurosci* 6:832–836.

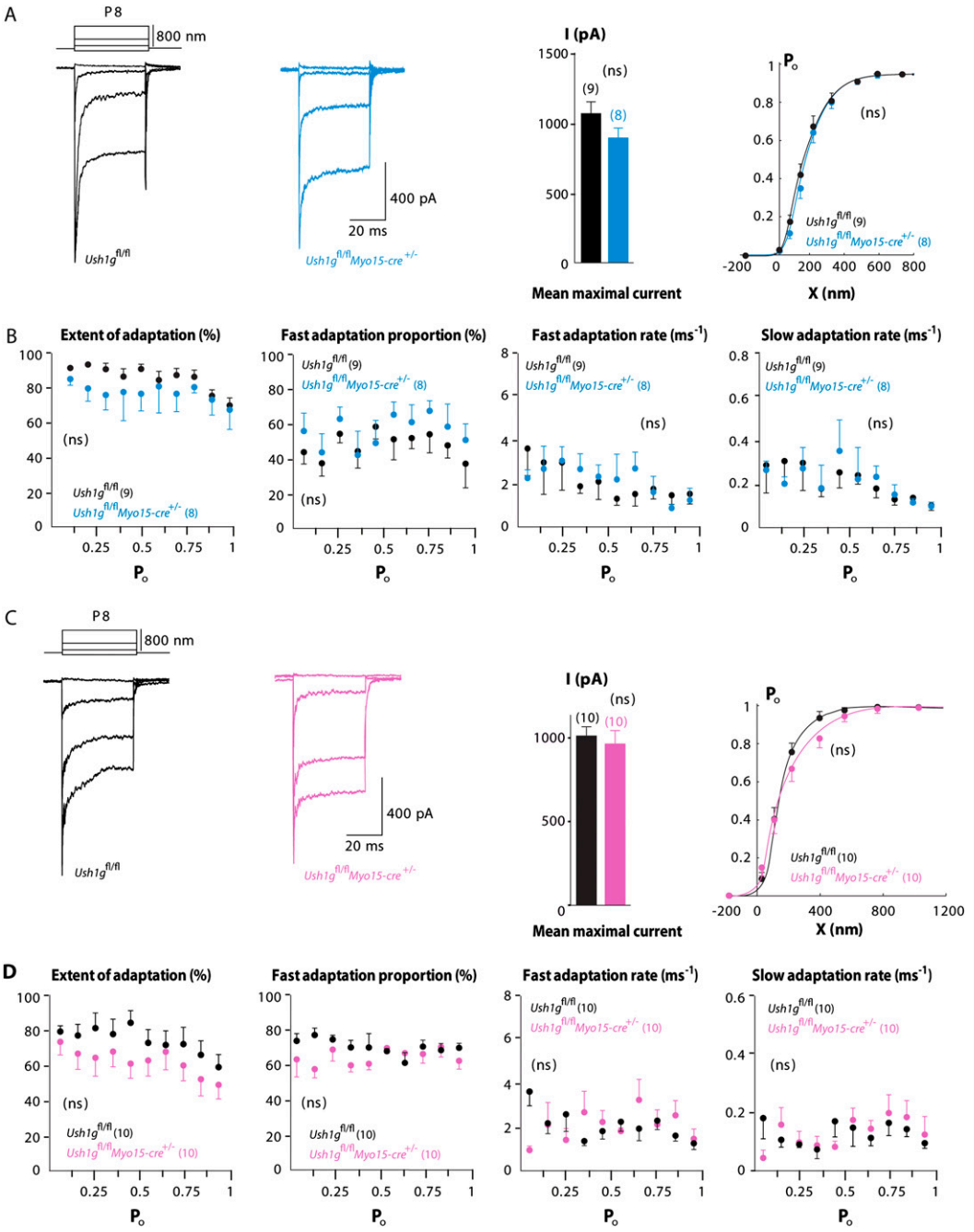

Fig. S7. Mechanoelectrical transduction current recordings in outer hair cells (OHCs) from *Ush1g*$^{fl/fl}$*Myo15-cre*$^{+/-}$ P8 mice. To test if hair cell function was affected despite the absence of morphological changes, we analyzed mechanoelectrical transduction currents at P8 in hair cells from the cochlear apical region (*A* and *B*: ~35% the total length of the cochlea from the apex) and the middle region (*C* and *D*: ~55% the total length) in *Ush1g*$^{fl/fl}$ and *Ush1g*$^{fl/fl}$ *Myo15-cre*$^{+/-}$ mice. (*A*) Examples of transduction currents in apical OHCs from *Ush1g*$^{fl/fl}$ (black) and *Ush1g*$^{fl/fl}$*Myo15-cre*$^{+/-}$ (blue) P8 mice. Mean maximum current amplitude is 1,014 ± 82 pA and 866 ± 67 pA for *Ush1g*$^{fl/fl}$ and *Ush1g*$^{fl/fl}$*Myo15-cre*$^{+/-}$ inner hair cells (IHCs), respectively (unpaired *t* test, $P = 0.19$). The $P_o(X)$ curves can be superimposed, with values of averaged sensitivity of 3.89 ± 0.38 μm^{-1} and 3.41 ± 0.18 μm^{-1} for *Ush1g*$^{fl/fl}$ and *Ush1g*$^{fl/fl}$*Myo15-cre*$^{+/-}$, respectively (unpaired *t* test, $P = 0.28$). In addition, no change in $X_{0.5}$ could be detected in the mutant OHCs, with values of 188 ± 23 nm and 196 ± 12 nm in *Ush1g*$^{fl/fl}$ and *Ush1g*$^{fl/fl}$*Myo15-cre*$^{+/-}$, respectively (unpaired *t* test, $P = 0.9$). (*B*) We characterized the adaptation in *Ush1g*$^{fl/fl}$ and *Ush1g*$^{fl/fl}$*Myo15-cre*$^{+/-}$ OHCs from the cochlear apex in terms of its extent and kinetics. We compared the extent of adaptation, the fast adaptation proportion, and the fast and slow adaptation rates in *Ush1g*$^{fl/fl}$ and *Ush1g*$^{fl/fl}$*Myo15-cre*$^{+/-}$ mice, and no change could be detected in the mutant OHCs (two-way ANOVA, $P = 0.51$, $P = 0.05$, $P = 0.73$, and $P = 0.96$, respectively). (*C*) Examples of transduction currents in an *Ush1g*$^{fl/fl}$ OHC (black) and an *Ush1g*$^{fl/fl}$*Myo15-cre*$^{+/-}$ OHC (pink) from the middle of the cochlea at P8. Mean maximum current amplitude is 963 ± 91 pA and 1,009 ± 60 pA for *Ush1g*$^{fl/fl}$ and *Ush1g*$^{fl/fl}$*Myo15-cre*$^{+/-}$ OHCs, respectively (unpaired *t* test, $P = 0.69$). The $P_o(X)$ curves can be superimposed with values of sensitivity 3.73 ± 0.27 μm^{-1} and 3.19 ± 0.70 μm^{-1} for *Ush1g*$^{fl/fl}$ and *Ush1g*$^{fl/fl}$*Myo15-cre*$^{+/-}$, respectively (unpaired *t* test, $P = 0.48$). In addition, no change in $X_{0.5}$ could be detected in the mutant IHCs, with values of 179 ± 19 nm and 213 ± 29 nm in *Ush1g*$^{fl/fl}$ and *Ush1g*$^{fl/fl}$*Myo15-cre*$^{+/-}$ IHCs, respectively (unpaired *t* test, $P = 0.34$). (*D*) We characterized the adaptation in *Ush1g*$^{fl/fl}$ and *Ush1g*$^{fl/fl}$*Myo15-cre*$^{+/-}$ OHCs from the middle in terms of its extent and kinetics. We compared the extent of adaptation, the fast adaptation proportion and the fast and slow adaptation rates in *Ush1g*$^{fl/fl}$ and *Ush1g*$^{fl/fl}$*Myo15-cre*$^{+/-}$ mice, and no change could be detected in the mutant OHCs (two-way ANOVA, $P = 0.5$, $P = 0.05$, $P = 0.91$, and $P = 0.96$, respectively).

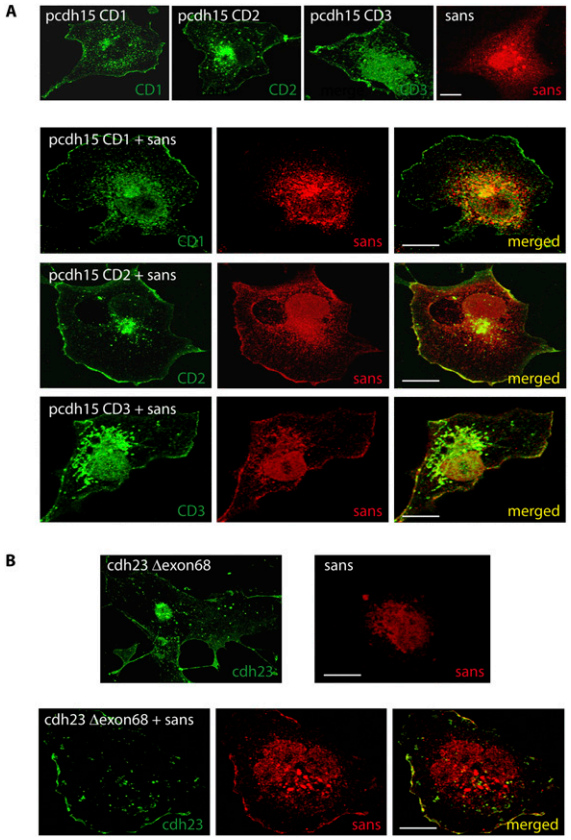

Fig. S8. Protocadherin-15 CD2 and CD3 and cadherin-23 colocalize with sans at the plasma membrane in cotransfected COS-7 cells. (*A*) COS-7 cells were transiently transfected to produce one of the protocadherin-15 (pcdh15) CD1, CD2, or CD3 isoforms and/or sans. In the single-transfected cells, protocadherin-15 CD1, CD2, and CD3, but not sans, are targeted to the plasma membrane. In cotransfected cells, sans is recruited at the plasma membrane only in cells that also produce protocadherin-15 CD2 or CD3, but not CD1. (*B*) COS-7 cells were transiently transfected to produce cadherin-23 (cdh23) and/or sans. In co-transfected cells producing sans and cadherin-23, sans is recruited at the plasma membrane, where it colocalizes with cadherin-23. (Scale bars: 5 μm.)